

Search for GeV Gamma-Ray Emission from SPT-SZ selected Galaxy Clusters with 15 years of Fermi-LAT data

Siddhant Manna^{1,*} and Shantanu Desai^{1,†}

¹ Department of Physics, IIT Hyderabad Kandi, Telangana 502284, India

Galaxy clusters could produce gamma-rays from inverse Compton scattering of cosmic ray electrons or hadronic interactions of cosmic ray protons with the intracluster medium. It is still an open question on whether gamma-ray emission ($>$ GeV energies) has been detected from galaxy clusters. We carry out a systematic search for gamma-ray mission based on 300 galaxy clusters selected from the 2500 deg.² SPT-SZ survey after sorting them in descending order of M_{500}/z^2 , using about 15 years of Fermi-LAT data in the energy range between 1-300 GeV. We were able to detect gamma-ray emission with significance of about 6.1σ from one cluster, viz SPT-CL J2012-5649. The estimated photon energy flux from this cluster is approximately equal to 1.3×10^{-6} MeV cm⁻² s⁻¹. The gamma-ray signal is observed between 1 – 10 GeV with the best-fit spectral index equal to -3.61 ± 0.33 . However, since there are six radio galaxies spatially coincident with SPT-CL J2012-5649 within the Fermi-LAT PSF, we cannot rule out the possibility this signal could be caused by some of these radio galaxies. Six other SPT-SZ clusters show evidence for gamma-ray emission with significance between $3 - 5\sigma$. None of the remaining clusters show statistically significant evidence for gamma-ray emission.

I. INTRODUCTION

Galaxy clusters are formed from the gravitational collapse of overdense regions in the early universe. As the universe evolves, the overdense regions created from density perturbations accumulate more matter due to gravity, forming clumps and filaments that eventually merge to form clusters [1]. Therefore, galaxy clusters constitute the largest gravitationally bound and virialized structures in the Universe and act as a unique laboratory to probe cosmology [2–4] and fundamental Physics [5–9]. Galaxy clusters have been observed over an extended wavelength range from radio waves [10] to hard X-rays [11]. Over the past two decades, a large number of dedicated surveys in optical, X-ray, and microwave have discovered many new galaxy clusters, which have been used for a plethora of Cosmology and Astrophysics studies, sometimes using a combination of observations at multiple wavelengths. However, at higher energies ($E > 1$ MeV), it is still an open question, as to whether gamma-rays have been observed from galaxy clusters. This work is focused on searching for gamma-ray emission from galaxy clusters using a mass limited catalog.

A number of mechanisms have been proposed for the production of gamma-rays within clusters, which we briefly recap. Galaxy clusters constitute high concentrations of galaxies, dark matter (about 80%), and hot diffuse gas (10-15%). They are also giant reservoirs of high energy relativistic cosmic rays (CRs), i.e. relativistic electrons and protons swarming in the hot ionized Intra-Cluster Medium (ICM) [12, 13]. Evidence for the acceleration of cosmic ray electrons comes from the observations of radio relics within clusters [13, 14]. These relics result from the shock waves

generated during cluster mergers, accelerating particles to extreme energies. These accelerated particles could produce gamma rays through Inverse Compton Scattering of relativistic electrons with the CMB, non-thermal bremsstrahlung, or through the decay of neutral pions produced from the collisions of cosmic ray protons with the intracluster medium (ICM) [15–22]. Most recently, the integrated gamma-ray flux from galaxy clusters has been calculated by combining cosmological MHD simulations of clusters of galaxies with the cosmic ray propagation in the redshift range $z \leq 5$, where it was shown that this integrated flux could contribute up to 100% of the diffuse gamma-ray flux $z \leq 5$ [23].

Since most of the mass in galaxy clusters is made up of non-baryonic cold dark matter, one could also detect gamma rays in clusters through the annihilation of dark matter WIMPs [24–28]. Besides the aforementioned mechanisms for gamma-ray emission from the ICM, one could also obtain gamma-ray emission from star formation activity in cluster member galaxies [29].

Before the launch of the Fermi Gamma-ray Space Telescope, the most definitive result on gamma-ray emission from galaxy clusters was reported in [30] using nine years of EGRET data from 1991–2000. This work reported upper limits for 58 X-ray-selected galaxy clusters for energies between 100 MeV – 30 GeV. In June 2008, NASA launched the Fermi Gamma-ray Space Telescope. The Large Area Telescope (LAT) is one of the two instruments onboard this detector. Fermi-LAT is sensitive to high energy gamma rays from various astrophysical sources. It is a pair-conversion telescope that is sensitive to photons between the energy range of 20 MeV to more than 300 GeV [31]. A plethora of studies have used the Fermi-LAT data to look for both diffuse broadband [32–44] and line emissions from galaxy clusters [45, 46]. We report a few salient highlights from some of the above works. Among all the above searches, no extended broad-band gamma-ray emission has been unambigu-

*Email:ph22resch11006@iith.ac.in

†Email:shntn05@gmail.com

ously detected from the cluster ICM, except for the Coma cluster. For all other clusters, any putative gamma-ray signal seen in searches from galaxy clusters has been attributed to AGNs (such as blazars) located inside the cluster [35, 47, 48]. A large number of works have looked for gamma-ray emission from the Coma cluster (Abell 1656) with Fermi-LAT. The discovery of a massive radio halo and radio remnants suggests efficient particle acceleration in the Coma Cluster [49]. Although initial searches by the Fermi-LAT Collaboration as well as by other authors found no statistically significant gamma-ray emission from the Coma cluster [24, 36, 40, 42], other works have found statistically significant emission from the Coma cluster with accumulated livetime. In 2017, a ring-like structure on the fringes of the Coma galaxy cluster was discovered using eight years of Fermi-LAT data with 3.4σ significance [50]. This detection was confirmed in [44] using nine years of Fermi-LAT data with the observed significance $> 5\sigma$, and reaffirmed in [51], who found extended diffuse gamma-ray emission with 5.4σ significance based on 12.3 years of data. The theoretical implications of this detection from Coma cluster are discussed in [52]. No significant emission was seen from the VIRGO cluster, although emission was detected from two elliptical galaxies, M87 and M49 located near the VIRGO center [41]. In addition to searches from the ICM, a search from 114 Brightest cluster galaxies (BCGs) selected from multiple X-ray catalogs, containing radio sources with flux above 50/75 mJy was done using 45 months of Fermi-LAT data [38]. This search detected signals from four possible sources, although none of them could be unambiguously associated with the BCGs [38].

In addition to the above pointed searches from individual clusters, many works have also done a stacking analysis from multiple clusters. The first such study looked for stacked emission from 53 clusters in the HIFLUGCS sample [53] and did not detect any significant emission [54]. A similar search was done using the Fermi-LAT data above 10 GeV by stacking 55 clusters from the HIFLUGCS sample [35]. A 4.3σ excess was obtained from this analysis, which was attributed to contribution from AGNs [35]. A similar stacking analysis of the Fermi-LAT data using 78 clusters ($z < 0.12$) from the 2MASS survey reported null results [39]. Another stacked search using 112 clusters in the MCXC catalogue found evidence at 5.8σ significance for a central point source dominated by AGN emission along with a gamma-ray ring at the position of the virial shock [55].

In addition to the aforementioned pointed or stacked searches from X-ray selected cluster samples, a novel search for gamma-ray emission was done by cross-correlating the cluster positions from SDSS and Planck selected clusters with the Fermi-LAT data, and calculating the two-point correlation function [43]. A positive correlation was seen from this search, attributed to cumulative emissions from AGNs. However, a definitive conclusion as to whether the cross-correlation is because of AGNs inside the

cluster or diffuse emission within the ICM could not be drawn [43].

Motivated by some of the above works, which found tantalizing hints for gamma-ray emission from clusters, we would like to systematically search the Fermi-LAT data using galaxy clusters detected using the Sunyaev-Zel'dovich (SZ) effect [56]. The SZ effect arises from the interaction of CMB photons with high energy electrons in galaxy clusters through Inverse Compton Scattering. The SZ effect is sensitive to the cluster mass threshold and is independent of redshift. Therefore SZ surveys provide a mass-limited catalog independent of redshift [57, 58].

This manuscript is structured as follows. In Sect. II, we describe the SPT-SZ cluster sample used for our analysis. In Sect. III, we explain the Fermi-LAT data analysis procedure used to search for gamma-ray emission. Our results are discussed in Sect. IV. Finally, our conclusions can be found in Sect. V. For our analysis, we assume a flat Λ CDM cosmology with $\Omega_m = 0.3$ and $h = 0.7$.

II. CLUSTER SELECTION

The dataset used for our analysis consists of galaxy clusters detected by the South Pole Telescope (SPT). The SPT is a 10-meter telescope located at the South Pole that has imaged the sky at three different frequencies: 95 GHz, 150 GHz, and 220 GHz [59]. SPT completed a 2500 square-degree survey between 2007 and 2011 to detect galaxy clusters using the SZ effect. This 2500 sq. degree SPT-SZ survey detected 677 confirmed galaxy clusters with SNR greater than 4.5, corresponding to a mass threshold of $3 \times 10^{14} M_\odot$ up to redshift of 1.8 [60, 61]¹. SPT has an angular resolution of approximately 1 arcminute [59]. The SPT cluster redshifts have been obtained using a dedicated optical and infrared follow-up campaign, consisting of pointed imaging and spectroscopic observations [62, 63], as well as using the data from optical surveys such as BCS [64] and DES [65]. The original SPT telescope has subsequently been upgraded with new instrumentation and has conducted additional cluster surveys using SPTPol [66], and in the future, will be superseded by SPT-3G [67]. Similar to [54], we carried out a search for gamma-ray emission from 300 clusters from the above sample in decreasing order of M_{500}/z^2 , where M_{500} is the total mass contained within a sphere with an average density equal to 500 times the critical density of the universe at the cluster's redshift and z is the cluster's redshift [61]. Note that this choice of ordering is arbitrary and we could have instead ordered it according to M_{500}/D_L^2 .

¹ https://pole.uchicago.edu/public/data/sptsz-clusters/2500d_cluster_sample_Bocquet19.fits

III. FERMI-LAT DATA ANALYSIS

We used the data from the Fermi-LAT Pass 8 ULTRACLEANVETO ('FRONT + BACK') class events [68] spanning almost 15 years of data (MET 239587201-710640005) from August 5, 2008 to July 10, 2023. This event class was chosen because it had the lowest amount of cosmic ray contamination, which makes it perfect for studying diffuse emissions. The data were chosen within a 5° radius around the cluster center (based on the SPT-derived position) between 1000 MeV and 300 GeV. Due to the large Point Spread Function (PSF) at lower energies, we avoided analyzing data below 1 GeV [68]. At the lowest energy of 1 GeV considered, the PSF is around 1.72° and for the highest energy considered of 300 GeV, the PSF is found to be 0.17° [69].

We used the `Fermipy` (version 1.2 [70]) and `FermiTools` v2.2.0 software packages to analyze the data using the binned maximum-likelihood analysis technique with the P8R3_ULTRACLEANVETO_V3 instrument response functions (IRFs). We used the `Fermibottle` Docker container and analysis environment provided by the Fermi Science Support Center.² The recommended (`DATA_QUAL > 0`) and (`LAT_CONFIG == 1`) data quality filters were used for the data reduction. For better quality data and more refinement, we also applied `abs(rock_angle) < 52°` and $|b| < 20^\circ$ as additional cuts. To further reduce contamination from the Earth's atmosphere, we used a zenith angle cut of 90° to the events. We used 0.2-pixel resolution for the spatial binning and 10 logarithmic energy bins per decade for the spectral binning in the energy range 1 GeV - 300 GeV.

A. Background Model

In our background model, we included all the sources from the fourth Fermi-LAT catalog of gamma-ray sources (4FGL-DR4), consisting of both point-like and extended sources [71]. To account for the diffuse emission, we used the Galactic diffuse emission model (`gll_iem_v07.fits`) with an isotropic component (`iso_P8R3_ULTRACLEANVETO_V3_v1.txt`) appropriate to the ULTRACLEANVETO event class. We allowed the normalization of the templates used to describe the Galactic foreground and isotropic diffuse emission to vary. The Fermi-LAT background models are divided into the Galactic diffuse model and the isotropic spectral template. The Galactic diffuse model consists of a spatial and spectral template that describes the emission from the Milky Way. The isotropic spectral template provides the spectral form from a fit to the all-sky emission not represented in the Galactic diffuse model.

B. Binned Likelihood Analysis

We used the conventional binned-likelihood analysis method outlined by the Fermi-LAT team to perform the likelihood analysis and model fitting. The spectral parameters of sources inside the region of interest (ROI) equal to 3° , were kept as free parameters during the fitting, whereas those for 4FGL-DR4 sources outside the ROI but within 5° were kept as constant during the fit. For our analysis, we utilize a point-source template for the gamma-ray detection with $\Gamma = 2$ similar to [51]. We used the software `gtselect` to select the events (gamma-ray photons) from the Fermi-LAT data based on multiple criteria such as the energy range, time span, ROI, and data quality. It enabled us to generate a filtered event file with the properties needed for our investigation. Utilizing the `gtmktime` function, we then generated a time filter for the Fermi-LAT data. This tool excluded time intervals with strong background activity, such as passes through the Earth's radiation belts or periods of sensor maintenance. Then, we generated a ROI counts map, summed over the photon energies, to identify candidate sources and validate that the field looks reasonable as a basic sanity check. For this purpose, we used the `gtbin` tool with the "CMAP" option. The data input for the binned likelihood analysis is a three-dimensional count map with an energy axis known as a counts cube. The counts cube is a square binned region displayed in the count's map that must fit within the circular acceptance cone defined during the data extraction. To calculate the exposure, we use the livetime cube, which is a three-dimensional array representing the time the LAT observed each position in the sky at each inclination angle and is required for precise flux and spectral analyses. It is created using the `gtltcube` software package. It adjusts for the exposure changes caused by the spacecraft's orbit and instrument livetime, and finally computes this exposure time as a function of energy for a region of interest.

Then, the source maps generated by `gtsrcmaps` are utilized for the likelihood analysis. These maps depict the projected counts from all sources within a specific energy range and spatial region. Finally, we generate the model maps using `gtmodel`. When the model closely aligns with the actual gamma-ray emissions in the observed region, the resulting model map should closely mirror the counts map.

C. Model fitting using Maximum Likelihood Estimate

We used Maximum Likelihood Estimate (MLE) to find the best-fit model parameters that describe the source's spectrum and position [72]. We use `gtlike` to carry out the binned likelihood analysis of the LAT data. It works by taking a model of the gamma-ray sky and calculating the probability of observing the data given that model. The model includes informa-

² available at <https://github.com/fermi-lat/FermiBottle>

tion about the locations, spectra, and other source properties. For source detection, we calculate the Test Statistic (TS) using `gttsmap` to characterize the significance of gamma-ray sources, which is given as follows:

$$TS = -2 \ln \left(\frac{L_{\max,0}}{L_{\max,1}} \right), \quad (1)$$

$L_{\max,0}$ corresponds to the null hypothesis (MLE for the model without the signal model), and $L_{\max,1}$ is the alternative hypothesis (signal model at the specified location). Wilks' Theorem states that for large counts, TS for the null hypothesis is asymptotically distributed as a χ^2 distribution [73]. The detection significance (or Z -score) is equal to \sqrt{TS} . This TS statistic is also widely used in neutrino astrophysics to quantify the detection significance [74].

IV. RESULTS

We implemented the aforementioned MLE procedure on 300 SPT-SZ galaxy clusters sorted in decreasing order of their M_{500}/z^2 values. These 300 clusters have been juxtaposed on the 12 year Fermi point-source catalogue skymap in galactic coordinates in Fig. 1.³ Our results from the MLE analysis for these clusters are tabulated in Table I. Each row contains the cluster M_{500} in units of $(\times 10^{14} M_\odot)/h$, redshift, RA, and declination, all of which were obtained from [60] and finally the corresponding TS value. For this sample of clusters, the virial radius of the clusters corresponds to a mean subtended angle $\theta_{200} = 0.039^\circ$ and corresponding standard deviation equal to 0.026° . We found only one cluster (SPT-CL J2012-5649) with detection significance $> 5\sigma$ (TS=37.2). In addition, there are six clusters with detection significance greater than 3σ . These clusters include SPT-CL J2021-5257 (TS=12), SPT-CL J0217-5245 (TS=11.9), SPT-CL J0232-5257 (TS=11.5), SPT-CL J0619-5802 (TS=10.3), SPT-CL J0124-4301 (TS=9), and SPT-CL J2140-5727 (TS=9) respectively. All other clusters had TS values < 9 (or $< 3\sigma$ significance).

We note two noteworthy merging clusters in our sample: the Bullet Cluster (SPT-CL J0658-5556) and El Gordo Cluster (SPT-CL J0102-4915). These have TS values of 2.1 and 4.7, respectively, corresponding to no significant excess. The Bullet cluster is a merging cluster that has been used to test Λ CDM and modified gravity theories [75]. The gamma-ray luminosity for the Bullet cluster has also been previously estimated in literature from the observed infrared luminosity, but was shown to be undetectable by Fermi-LAT due to its large redshift [29]. The

Fermi-LAT collaboration also did not find evidence for gamma-ray emission from the Bullet cluster using the first 1.5 years of data [32]. The El Gordo cluster is one of the most massive merging galaxy clusters ($M_{200} \sim 3 \times 10^{15} M_\odot$) located at a redshift of 0.87 [76] which has also been extensively used to test Λ CDM [77]. Therefore, there is no evidence for gamma-ray emission from these two merging clusters using 15 years of data.

We now discuss the results for the clusters with observed detection significance $> 3\sigma$. We first focus on SPT-CL J2012-5649 in detail, followed by the other clusters.

A. SPT-CL J2012-5649

We found a distinctive gamma-ray emission signature for SPT-CL J2012-5649. This cluster is located at a redshift of 0.055, SPT S/N ratio of 5.99, corresponding to $M_{500} \approx 5 \times 10^{14} M_\odot$ and angular diameter given by $\theta_{200} = 0.19^\circ$.

The TS map for SPT-CL J2012-5649 using a power law point source template with the photon spectral index $\Gamma = -2$, after smoothening with a Gaussian kernel ($\sigma = 1.5$) can be found in Fig. 2. This cluster has a TS value of around 37.2, corresponding to a detection significance of 6.1σ for this point source template. The observed signal is confined to about $0.2R_{200}$. We found no extended sources in our search. We also show the count maps and residuals in Fig. 3. The top panel shows the observed photons in the energy bins from 1-300 GeV along with the total signal, given by the sum of 4FGL-DR4 sources, galactic diffuse emission templates, and the observed emission from SPT-CL J2012-5649, whereas the fractional residuals determined from the full ROI of 5° for SPT-CL J2012-5649 are shown in the bottom panel. In Fig. 4, we depict the Gaussian kernel smoothed count map ($\sigma = 1.5$). The total photon flux for this cluster is equal to $(0.39 \pm 0.05) \times 10^{-9} \text{ ph cm}^{-2} \text{ s}^{-1}$ and the total energy flux corresponds to $(0.63 \pm 0.09) \times 10^{-6} \text{ MeV cm}^{-2} \text{ s}^{-1}$. In Fig. 5, we showcase the observed Spectral Energy Distribution (SED) for SPT-CL J2012-5649 along with the best-fit spectrum. We found the best-fit spectral index (γ) given by $\gamma = -3.61 \pm 0.33$, where $\frac{dN}{dE} \propto E^\gamma$. All the observed signal is between 1-10 GeV. For energy > 10 GeV, we only obtain upper limits. We also note that the fitted spectral index is independent of the choice of the spectral index used for the point source template.

For this cluster, we also did a search with other templates. For a radial disk and radial Gaussian templates, we found the TS value around 5.61 (2.36 σ). We also did a search in the energy range between 10 GeV to 300 GeV, we found the TS value to decrease significantly to 6.0 (2.4 σ). This is in accord with the observed SED which does not show any detections beyond 10 GeV.

³ For generating Fig. 1, we have used the FITS file available at https://fermi.gsfc.nasa.gov/ssc/data/access/lat/12yr_catalog/intens_scaled_ait_144m_gt1000_psf3_gal_0p1.fits.gz.

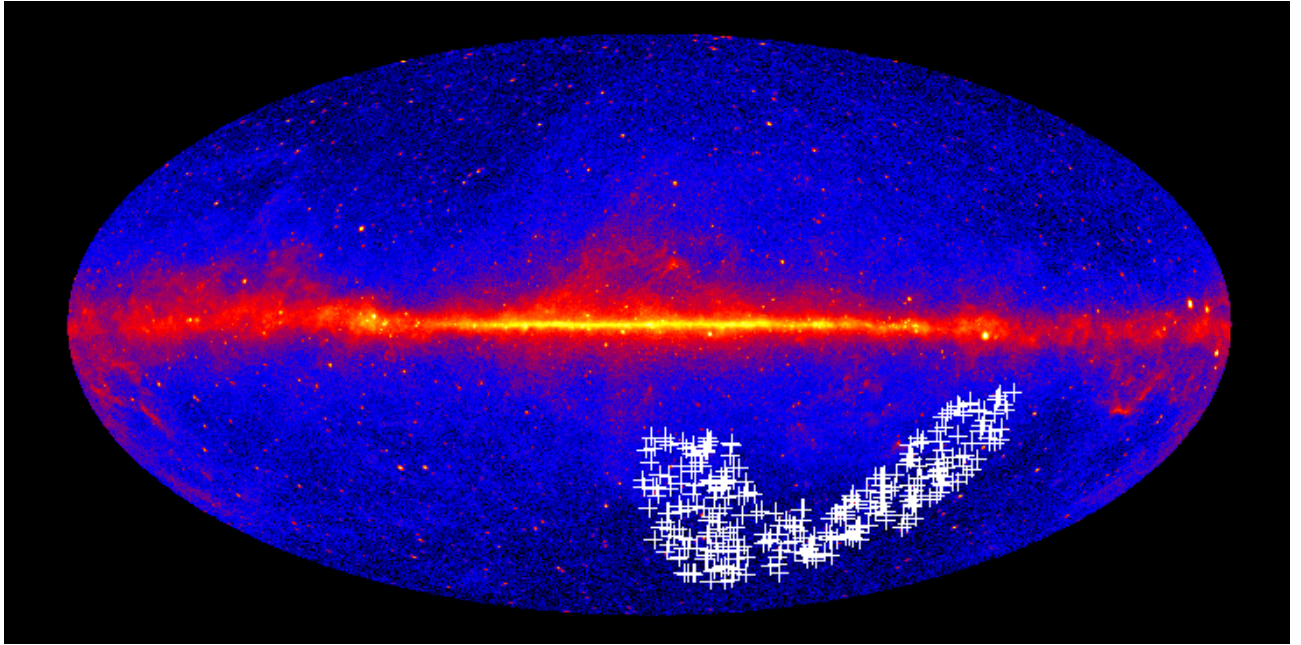


FIG. 1: The Fermi-LAT count map in galactic coordinates based on the 4FGL-DR4 catalog, using 12 years of survey data [71, 78]. The white colored plus sign depicts the locations of the 300 SPT-SZ galaxy clusters we used in our analysis. The bright, diffuse glow running along the middle of the map, shows the central plane of our Milky Way galaxy.

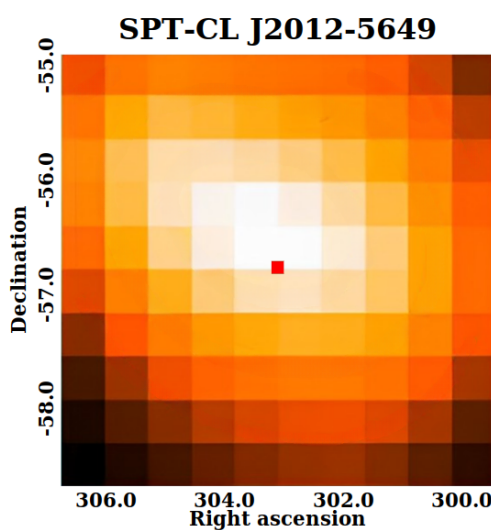


FIG. 2: Gaussian kernel smoothed ($\sigma = 1.5$) TS map of the SPT-CL J2012-5649 cluster (left) and TS map scale (right) generated using `gttsmap` in the energy band 1–300 GeV. We used 0.2-pixel resolution for the spatial binning. The red square shows the SPT cluster center.

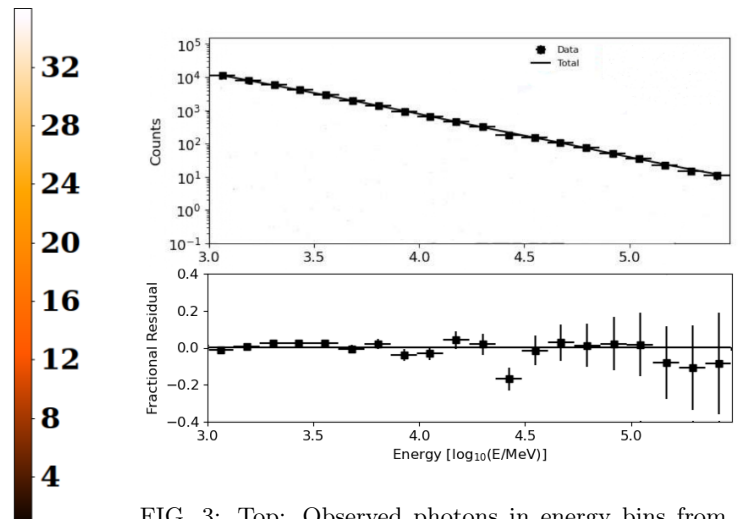


FIG. 3: Top: Observed photons in energy bins from 1–300 GeV and the cumulative model of the total emission all the 4FGL-DR4 source diffuse emission templates and the observed signal from SPT-CL J2012-5649. Bottom: The fractional residuals given by $(\text{counts}-\text{model})/\text{model}$, determined within 5° for SPT-CL J2012-5649.

SPT-CL J2012-5649 is spatially coincident with Abell 3667. Abell 3667 is also one of the most active galaxy clusters, with several ongoing mergers and collisions between galaxies. It is one of the brightest X-ray sources in the southern sky [79]. One of the most striking features of Abell 3667 is the large shock wave propagating through it. This shock wave was created when two smaller galaxy clusters collided

and merged to form Abell 3667 [80, 81]. The shock wave accelerates particles, creating a population of relativistic electrons emitting radio waves. Two giant radio relics, that are thought to be caused from the acceleration of electrons by the shock wave have also been detected within this cluster with ATCA and MeerKAT [80–82]. From the MeerKAT data, the presence of a pair of radio relics in the galaxy cluster Abell 3667 was reported [80]. The North Western (NW) radio relic has an angular size of 0.6° and an extension of 2.3 Mpc. The South Eastern (SE) relic is compar-

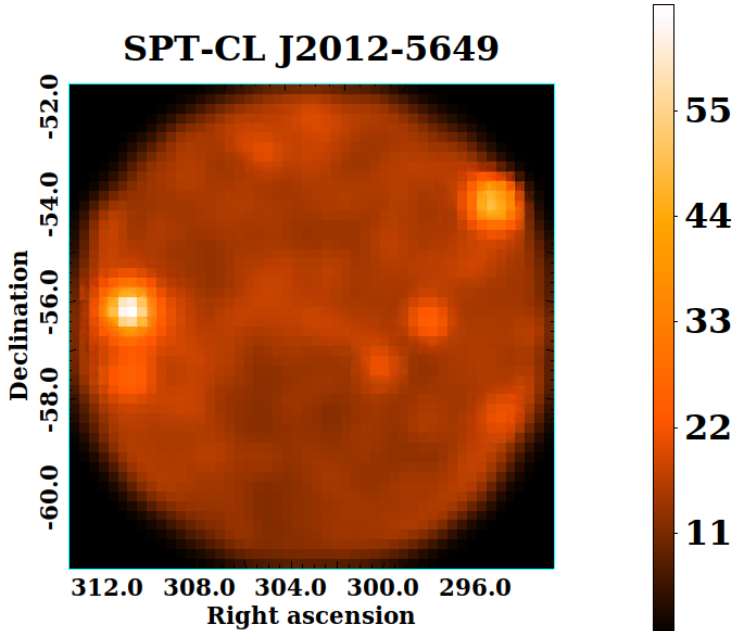


FIG. 4: Gaussian kernel smoothed ($\sigma = 1.5$) counts map of SPT-CL J2012-5649 cluster (left) generated using `gttsmap` in the energy range 1 – 300 GeV. We used 0.2-pixel resolution for the spatial binning.

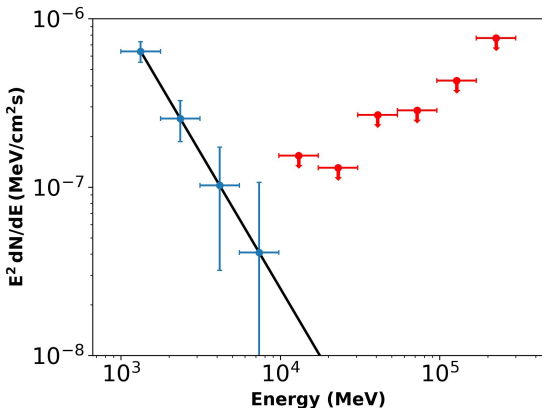


FIG. 5: The differential energy spectrum from SPT-CL J2012-5649 obtained using `easyFermi`. The solid line shows the power-law fit with the best-fit spectral index given by $\gamma = -3.61 \pm 0.329$. The blue data points show the measured differential energy spectrum, while the red point represent upper limits. All the signal is observed at energies ≤ 10 GeV, and beyond that we obtain upper limits.

atively smaller, with an angular size of 0.42° , and an extension of 1.6 Mpc. Furthermore, ATCA data was used to reveal the expansive nature of the NW radio relic, determining its total extent to be 2.6 Mpc [83]. This suggests that their angular sizes are comparable with the PSF of Fermi-LAT. It would be intriguing to correlate the gamma-ray flux with the radio flux and to redo our analysis using a template obtained from observations of this radio relic, similar to studies done for the Coma cluster [44]. One could also

estimate the observed gamma-ray flux for this cluster using the MINOT software [84]. These analyses shall be deferred to future work.

We, however, caution that any possible gamma-ray signals from galaxy clusters could be due to contamination by radio galaxies and blazars within the clusters. Fermi-LAT has detected gamma rays from radio galaxies at the centers of VIRGO and Perseus clusters [47, 48]. Furthermore, the MeerKAT observations of this cluster have revealed three radio galaxies within six arcminutes of the cluster center [80]. Therefore, to check for such a contribution, we searched for coincident radio sources using the Sydney University Molonglo Sky Survey (SUMSS) catalog [85]. Fermi-LAT has also detected GeV emission from radio galaxies and AGNs, including from SUMSS sources [86]. Within 0.2° , we found six SUMSS radio sources: SUMSS J201156-564547 with 17.5 mJy integrated 36-cm flux density, SUMSS J201142-564759 with 47.3 mJy integrated 36-cm flux density, SUMSS J201127-564358 with 535.7 mJy integrated 36-cm flux density, SUMSS J201125-564312 with 495.1 mJy integrated 36-cm flux density, SUMSS J201113-565408 with 13.4 mJy integrated 36-cm flux density, SUMSS J201317-565906 with 8.3 mJy integrated 36-cm flux density. These SUMSS sources have been classified as radio galaxies in SIMBAD, and are also within 10 arcminute from the three MeerKAT detected radio galaxies.

Therefore, our results imply a 6σ detection of gamma-rays from this cluster, which prima-facie is only the second cluster (after Coma) with statistical significance $> 5\sigma$. Nevertheless, since we found six SUMSS radio sources within the Fermi-LAT PSF, we cannot arbitrate as to whether the observed gamma-ray emission within this cluster is due to physical processes within the ICM or due to contamination from these radio sources. To the best of our knowledge, there has not been any previous result related to gamma-ray emission for this cluster using Fermi-LAT. However, a search for TeV gamma rays was done from Abell 3667 using the CANGAROO-III atmospheric Cherenkov telescope, which reported null results [87].

B. Clusters with significance between 3 – 5σ

We now discuss the remaining six clusters with significance greater than 3σ . These clusters include SPT-CL J2021-5257, SPT-CL J0217-5245, SPT-CL J0232-5257, SPT-CL J0619-5802, SPT-CL J0124-4301, and SPT-CL J2140-5727. The count maps after smoothening with a Gaussian kernel ($\sigma = 1.5$) are depicted in Figures 6, 7, 8, 9, 10, and 11, respectively. We have shown their corresponding TS maps after smoothening with a Gaussian kernel in Figures 15, 16, 17, 18, 19, and 20 respectively. For three of these clusters, SPT-CL J0217-5245, SPT-CL J0619-5802 and SPT-CL J2140-5727, we were able to find the counterparts SUMSS J021714-524528, SUMSS J061941-580217 and SUMSS J214034-572717, respectively in the SUMSS radio source catalogue within one arcminute, with the

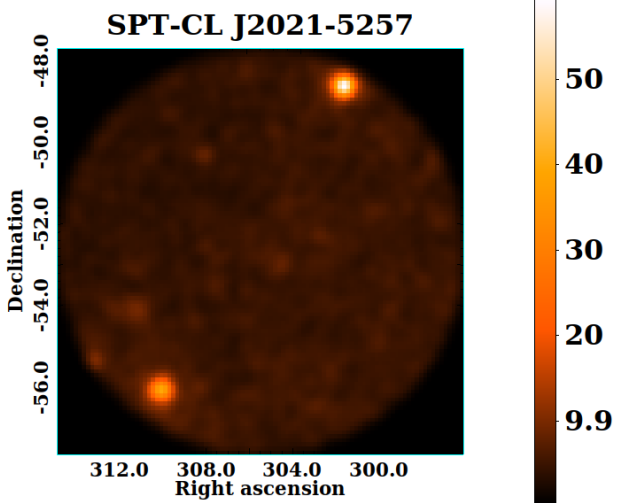


FIG. 6: Gaussian kernel smoothed counts map of the SPT-CL J2021-5257 cluster done in the same way as in Fig. 4.

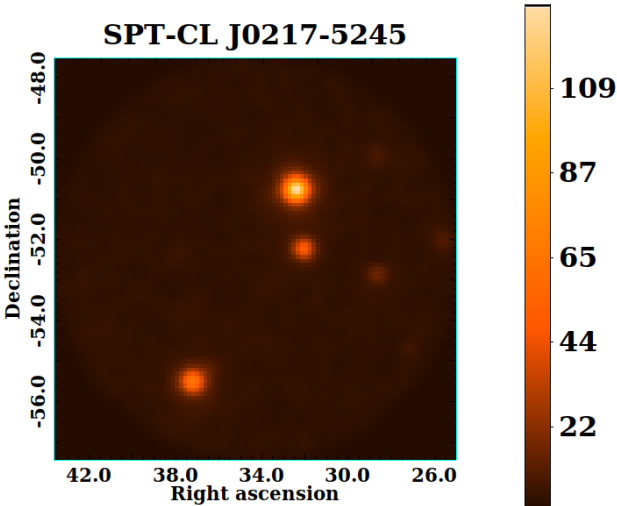


FIG. 7: Gaussian kernel smoothed counts map of the SPT-CL J0217-5245 cluster done in the same way as in Fig. 4.

integrated 36-cm flux density of these sources equal to 23.5 mJy, 33.2 mJy, and 9.0 mJy, respectively. These radio sources have also been classified as radio galaxies and could contribute to the observed emission for these clusters.

V. CONCLUSIONS

In this work, we have searched for gamma-ray emission with energies between 1-300 GeV from galaxy clusters, selected from the SPT-SZ 2500 sq. degree survey. For this purpose, we used 15 years of Fermi-LAT data and point-source templates for these searches. This analysis was done using 300 SPT-SZ galaxy clusters, after sorting them in descending order based on their M_{500}/z^2 values. Among these clusters, we found statistically significant emission from SPT-CL J2012-5649 (Abell 3667) with a detection signifi-

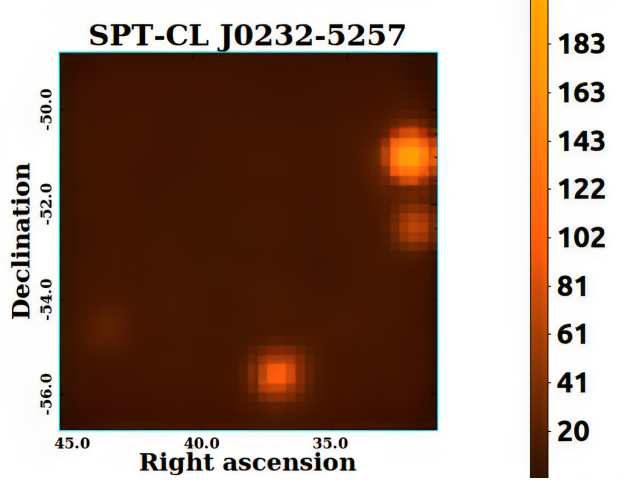


FIG. 8: Gaussian kernel smoothed counts map of the SPT-CL J0232-5257 cluster done in the same way as in Fig. 4.

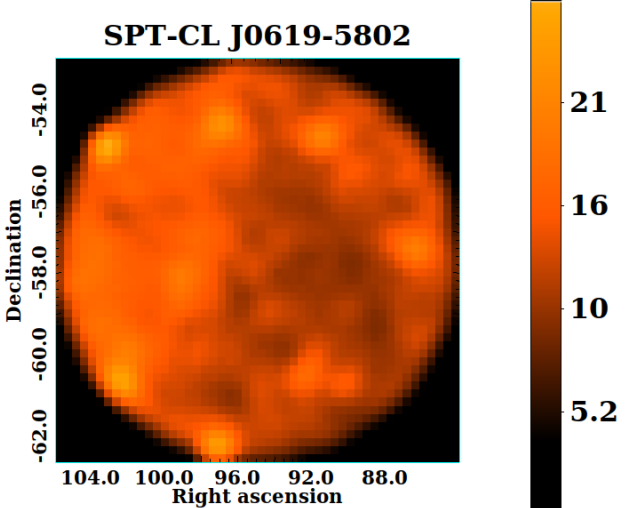


FIG. 9: Gaussian kernel smoothed counts map of the SPT-CL J0619-5802 cluster done in the same way as in Fig. 4.

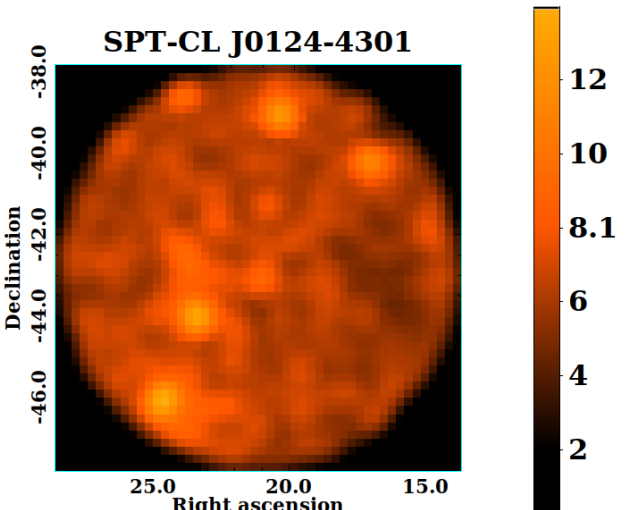


FIG. 10: Gaussian kernel smoothed counts map of the SPT-CL J0124-4301 cluster done in the same way as in Fig. 4

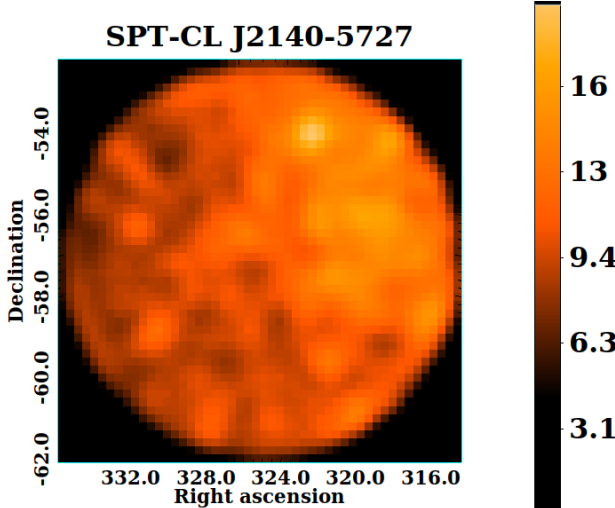


FIG. 11: Gaussian kernel smoothed counts map of the SPT-CL J2140-5727 cluster done in the same way as in Fig. 4.

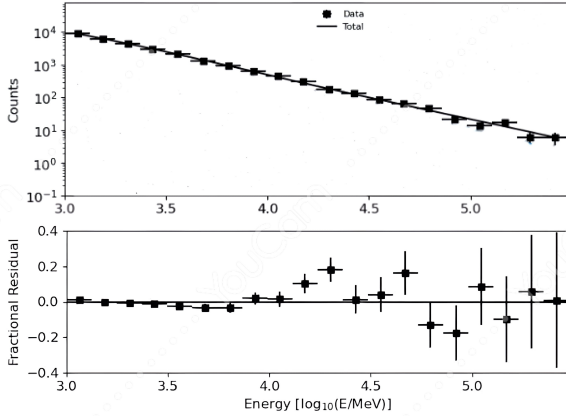


FIG. 12: Observed photons and residuals for SPT-CL J2021-5257 in the energy range 1 GeV to 300 GeV. This plot uses the same specifications as in Fig. 3.

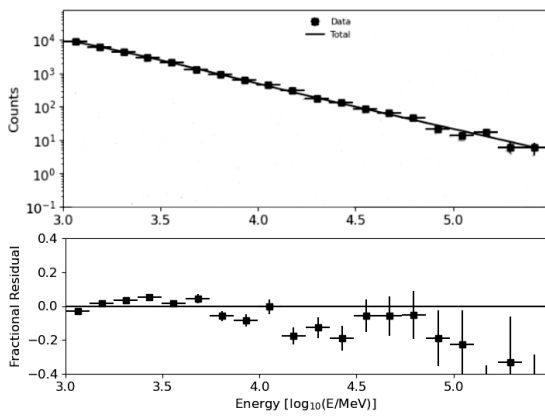


FIG. 13: Observed photons and residuals for SPT-CL J0619-5802 in the energy range 1 GeV to 300 GeV. This plot uses the same specifications as in Fig. 3.

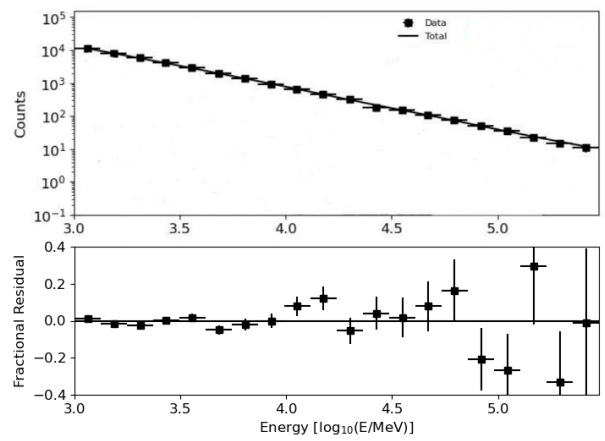


FIG. 14: Observed photons and residuals for SPT-CL J0217-5245 in the energy range 1 GeV to 300 GeV. This plot uses the same specifications as in Fig. 3.

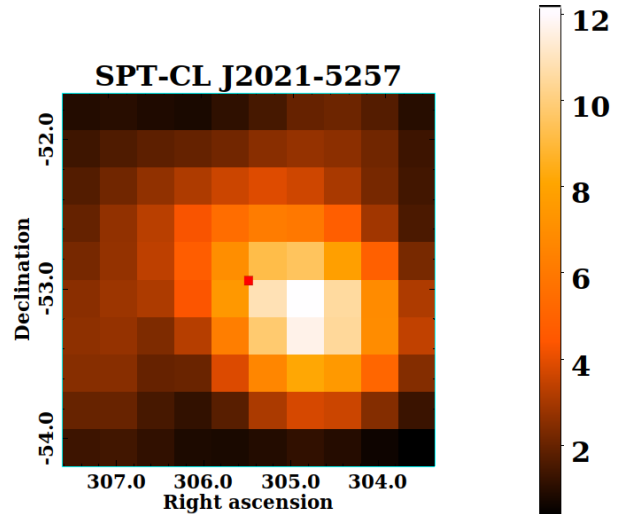


FIG. 15: Gaussian kernel smoothed TS map of the SPT-CL J2021-5257 cluster done in the same way as Fig. 2.

cance of 6.1σ . This signal is confined to $0.2R_{200}$. The total photon flux is approximately equal to 1.3×10^{-10} ph cm^{-2} s^{-1} with the total energy flux $\sim 1.3 \times 10^{-6}$ MeV cm^{-2} s^{-1} . This cluster is a merging cluster for which radio relics have been detected using MeerKAT observations. The detection significance reduces to about 2.5σ if we use non-point source templates or search in a higher energy range from 10 to 300 GeV. The SED for this cluster can be found in Fig. 5. The signal is observed upto 10 GeV, while the spectral index is equal to -3.61 ± 0.33 . Above 10 GeV, we only obtain upper limits, which is consistent with the results from the MLE analysis in this energy range. Although prima-facie, this constitutes only the second galaxy cluster after Coma with detection significance $> 5\sigma$ at GeV energies, we note that there are six radio galaxies from the SUMSS catalogue within 0.2° of this cluster, which is within the Fermi-LAT PSF at this energy. Therefore, we cannot definitely con-

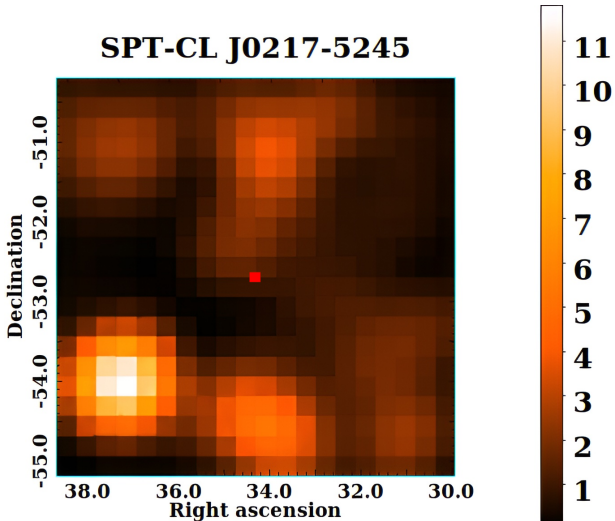


FIG. 16: Gaussian kernel smoothed TS map of the SPT-CL J0217-5245 cluster done in the same way as Fig. 2.

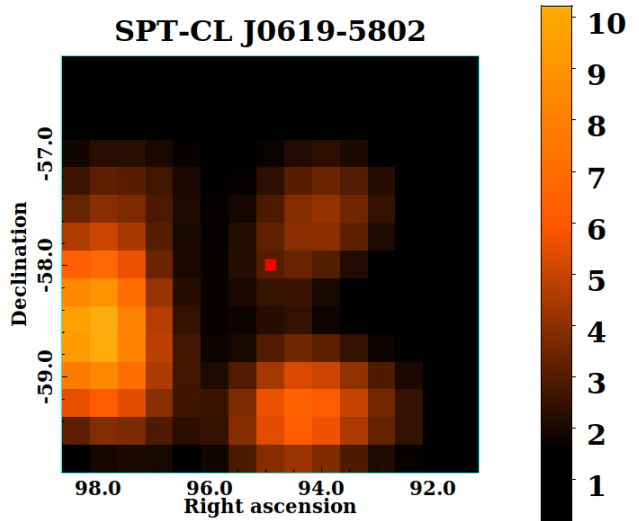


FIG. 18: Gaussian kernel smoothed TS map of the SPT-CL J0619-5802 cluster done in the same way as Fig. 2.

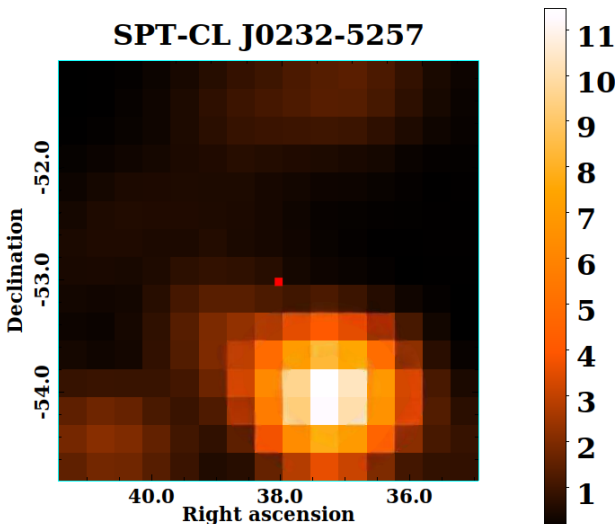


FIG. 17: Gaussian kernel smoothed TS map of the SPT-CL J0232-5257 cluster done in the same way as Fig. 2.

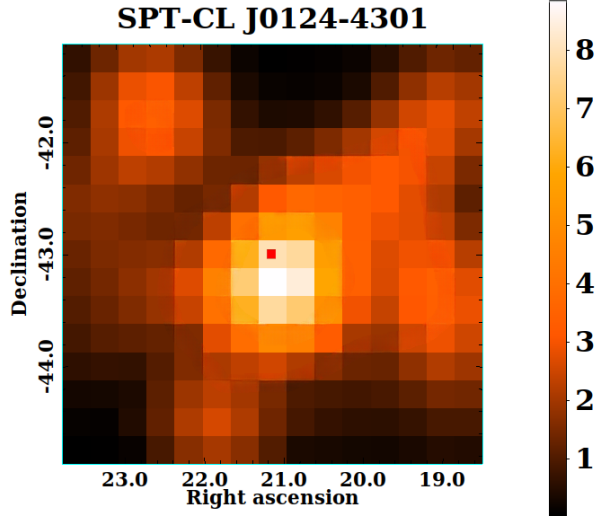


FIG. 19: Gaussian kernel smoothed TS map of the SPT-CL J1024-4301 cluster done in the same way as Fig. 2.

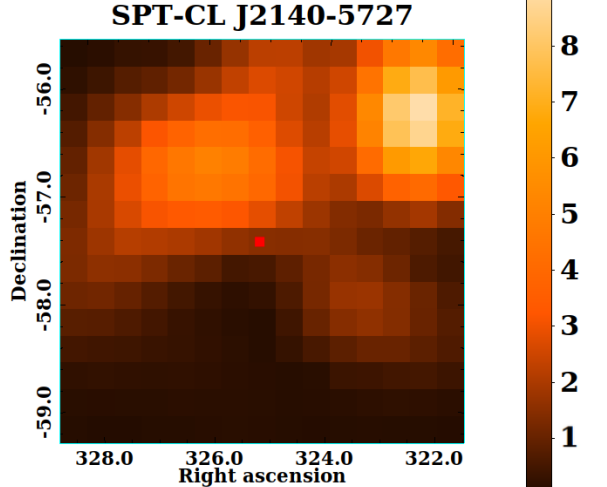


FIG. 20: Gaussian kernel smoothed TS map of the SPT-CL J2140-5727 cluster done in the same way as Fig. 2.

clude that the gamma-ray emission detected for SPT-CL J2012-5649 is coming from the ICM as opposed to radio sources contributing to this emission.

We also found six other clusters with significance between $3-5\sigma$. These clusters include SPT-CL J2021-5257, SPT-CL J0217-5245, SPT-CL J0232-5257, SPT-CL J1024-4301, SPT-CL J0619-5802, and SPT-CL J2140-5727. For three of these clusters (SPT-CL J0217-5245, SPT-CL J0619-5802 and SPT-CL J2140-5727) we again found three SUMSS radio galaxies within one arcminute. None of the remaining clusters show any evidence of gamma-ray emission. Two of these clusters (with null results) include the Bullet and El Gordo clusters.

In future works, we shall extend this analysis to all the SPT-SZ clusters (including those from SPTPol), redo the search with other search templates, using the observed radio emission as well as from dark matter

annihilations.

Acknowledgments

We also appreciate the invaluable contributions of the Fermi-LAT team for making the Fermi-LAT data and analysis codes publicly available and answering all our queries. Without their state-of-the-art analysis technique, this research would not have been possible. We acknowledge the National Supercomputing

Mission (NSM) for providing computing resources of ‘PARAM SEVA’ at IIT, Hyderabad, which is implemented by C-DAC and supported by the Ministry of Electronics and Information Technology (MeitY) and Department of Science and Technology (DST), Government of India. This research has used SAOImageDS9, developed by Smithsonian Astrophysical Observatory and we also thank them. We would also like to thank `easyFermi` team [88] and `Fermipy` team [70] for their software and support.

-
- [1] S. D. M. White and M. J. Rees, *MNRAS* **183**, 341 (1978).
 - [2] A. V. Kravtsov and S. Borgani, *Ann. Rev. Astron. Astrophys.* **50**, 353 (2012), 1205.5556.
 - [3] S. W. Allen, A. E. Evrard, and A. B. Mantz, *Ann. Rev. Astron. Astrophys.* **49**, 409 (2011), 1103.4829.
 - [4] A. A. Vikhlinin, A. V. Kravtsov, M. L. Markevitch, R. A. Sunyaev, and E. M. Churazov, *Physics Uspekhi* **57**, 317-341 (2014).
 - [5] H. Böhringer and G. Chon, *Modern Physics Letters A* **31**, 1640008 (2016), 1610.02855.
 - [6] S. Desai, *Physics Letters B* **778**, 325 (2018), 1708.06502.
 - [7] K. Bora and S. Desai, *JCAP* **2021**, 012 (2021), 2008.10541.
 - [8] K. Bora and S. Desai, *JCAP* **2021**, 052 (2021), 2104.00974.
 - [9] K. Bora, R. F. L. Holanda, S. Desai, and S. H. Pereira, *European Physical Journal C* **82**, 17 (2022), 2106.15805.
 - [10] L. Feretti, G. Giovannini, F. Govoni, and M. Murgia, *JCAP* **20**, 54 (2012), 1205.1919.
 - [11] D. R. Wik, A. Hornstrup, S. Molendi, G. Madejski, F. A. Harrison, A. Zoglauer, B. W. Grefenstette, F. Gastaldello, K. K. Madsen, N. J. Westergaard, et al., *Astrophys. J.* **792**, 48 (2014), 1403.2722.
 - [12] G. Brunetti and T. W. Jones, *International Journal of Modern Physics D* **23**, 1430007-98 (2014), 1401.7519.
 - [13] D. Wittor, *Universe* **9**, 319 (2023).
 - [14] S. Paul, R. Kale, A. Datta, A. Basu, S. Sur, V. Parekh, P. Gupta, S. Chatterjee, S. Salunkhe, A. Iqbal, et al., *Journal of Astrophysics and Astronomy* **44**, 38 (2023), 2211.01393.
 - [15] T. A. Ensslin, P. L. Biermann, P. P. Kronberg, and X.-P. Wu, *Astrophys. J.* **477**, 560 (1997), astro-ph/9609190.
 - [16] J. A. Hinton, W. Dominko, and E. C. D. Pope, *MNRAS* **382**, 466 (2007), astro-ph/0701033.
 - [17] A. Pinzke and C. Pfrommer, *MNRAS* **409**, 449 (2010), 1001.5023.
 - [18] F. Vazza, M. Brüggen, D. Wittor, C. Gheller, D. Eckert, and M. Stubbe, *MNRAS* **459**, 70 (2016), 1603.02688.
 - [19] V. Petrosian, *Astrophys. J.* **557**, 560 (2001), astro-ph/0101145.
 - [20] G. Brunetti, S. Zimmer, and F. Zandanel, *MNRAS* **472**, 1506 (2017), 1707.02085.
 - [21] G. Brunetti and A. Lazarian, *MNRAS* **410**, 127 (2011), 1008.0184.
 - [22] S. Hussain, G. Pagliaroli, and E. M. de Gouveia Dal Pino, arXiv e-prints arXiv:2307.15851 (2023), 2307.15851.
 - [23] S. Hussain, R. Alves Batista, E. M. de Gouveia Dal Pino, and K. Dolag, *Nature Communications* **14**, 2486 (2023), 2203.01260.
 - [24] M. Ackermann, M. Ajello, A. Allafort, L. Baldini, J. Ballet, G. Barbiellini, D. Bastieri, K. Bechtol, R. Bellazzini, R. D. Blandford, et al., *JCAP* **2010**, 025 (2010), 1002.2239.
 - [25] M. Di Mauro, J. Pérez-Romero, M. A. Sánchez-Conde, and N. Fornengo, *Phys. Rev. D* **107**, 083030 (2023), 2303.16930.
 - [26] T. Bringmann and C. Weniger, *Physics of the Dark Universe* **1**, 194 (2012), 1208.5481.
 - [27] M. Lisanti, S. Mishra-Sharma, N. L. Rodd, and B. R. Safdi, *Phys. Rev. Lett.* **120**, 101101 (2018), 1708.09385.
 - [28] D. Song, K. Murase, and A. Kheirandish, arXiv e-prints arXiv:2308.00589 (2023), 2308.00589.
 - [29] E. M. Storm, T. E. Jeltema, and S. Profumo, *Astrophys. J.* **755**, 117 (2012), 1206.1676.
 - [30] O. Reimer, M. Pohl, P. Sreekumar, and J. R. Mattox, *Astrophys. J.* **588**, 155 (2003), astro-ph/0301362.
 - [31] W. B. Atwood, A. A. Abdo, M. Ackermann, W. Antolini, B. Anderson, M. Axelsson, L. Baldini, J. Ballet, D. L. Band, G. Barbiellini, et al., *Astrophys. J.* **697**, 1071 (2009), 0902.1089.
 - [32] M. Ackermann, M. Ajello, A. Allafort, L. Baldini, J. Ballet, G. Barbiellini, D. Bastieri, K. Bechtol, R. Bellazzini, R. D. Blandford, et al., *Astrophys. J. Lett.* **717**, L71 (2010), 1006.0748.
 - [33] T. Arlen, T. Aune, M. Beilicke, W. Benbow, A. Bouvier, J. H. Buckley, V. Bugaev, K. Byrum, A. Cannon, A. Cesarini, et al., *Astrophys. J.* **757**, 123 (2012), 1208.0676.
 - [34] J. Han, C. S. Frenk, V. R. Eke, L. Gao, S. D. M. White, A. Boyarsky, D. Malyshev, and O. Ruchayskiy, *MNRAS* **427**, 1651 (2012), 1207.6749.
 - [35] D. A. Prokhorov and E. M. Churazov, *Astron. & Astrophys.* **567**, A93 (2014), 1309.0197.
 - [36] D. A. Prokhorov, *MNRAS* **441**, 2309 (2014).
 - [37] M. Ackermann, M. Ajello, A. Albert, A. Allafort, W. B. Atwood, L. Baldini, J. Ballet, G. Barbiellini, D. Bastieri, et al., *Astrophys. J.* **787**, 18 (2014), 1308.5654.
 - [38] K. L. Dutson, R. J. White, A. C. Edge, J. A. Hinton, and M. T. Hogan, *MNRAS* **429**, 2069 (2013), 1211.6344.
 - [39] R. D. Griffin, X. Dai, and C. S. Kochanek, *Astrophys. J. Lett.* **795**, L21 (2014), 1405.7047.

- [40] F. Zandanel and S. Ando, MNRAS **440**, 663 (2014), 1312.1493.
- [41] M. Ackermann, M. Ajello, A. Albert, W. B. Atwood, L. Baldini, G. Barbiellini, D. Bastieri, K. Bechtol, R. Bellazzini, E. Bissaldi, et al., Astrophys. J. **812**, 159 (2015), 1510.00004.
- [42] M. Ackermann, M. Ajello, A. Albert, W. B. Atwood, L. Baldini, J. Ballet, G. Barbiellini, D. Bastieri, K. Bechtol, R. Bellazzini, et al., Astrophys. J. **819**, 149 (2016), 1507.08995.
- [43] E. Branchini, S. Camera, A. Cuoco, N. Fornengo, M. Regis, M. Viel, and J.-Q. Xia, Astrophys. J. Suppl. Ser. **228**, 8 (2017), 1612.05788.
- [44] S.-Q. Xi, X.-Y. Wang, Y.-F. Liang, F.-K. Peng, R.-Z. Yang, and R.-Y. Liu, Phys. Rev. D **98**, 063006 (2018).
- [45] Y.-F. Liang, Z.-Q. Shen, X. Li, Y.-Z. Fan, X. Huang, S.-J. Lei, L. Feng, E.-W. Liang, and J. Chang, Phys. Rev. D **93**, 103525 (2016), 1602.06527.
- [46] B. Anderson, S. Zimmer, J. Conrad, M. Gustafsson, M. Sánchez-Conde, and R. Caputo, JCAP **2016**, 026 (2016), 1511.00014.
- [47] A. A. Abdo, M. Ackermann, M. Ajello, W. B. Atwood, M. Axelsson, L. Baldini, J. Ballet, G. Barbiellini, M. G. Baring, D. Bastieri, et al., Astrophys. J. **707**, 1310 (2009), 0910.4881.
- [48] A. A. Abdo, M. Ackermann, M. Ajello, K. Asano, L. Baldini, J. Ballet, G. Barbiellini, D. Bastieri, B. M. Baughman, K. Bechtol, et al., Astrophys. J. **699**, 31 (2009), 0904.1904.
- [49] G. Giovannini, L. Feretti, T. Venturi, K. T. Kim, and P. P. Kronberg, Astrophys. J. **406**, 399 (1993).
- [50] U. Keshet and I. Reiss, Astrophys. J. **869**, 53 (2018), 1709.07442.
- [51] V. Baghmanyan, D. Zargaryan, F. Aharonian, R. Yang, S. Casanova, and J. Mackey, MNRAS **516**, 562 (2022), 2110.00309.
- [52] R. Adam, H. Goksu, S. Brown, L. Rudnick, and C. Ferrari, Astron. & Astrophys. **648**, A60 (2021), 2102.02251.
- [53] Y. Chen, T. H. Reiprich, H. Böhringer, Y. Ikebe, and Y. Y. Zhang, Astron. & Astrophys. **466**, 805 (2007), astro-ph/0702482.
- [54] B. Huber, C. Tchernin, D. Eckert, C. Farnier, A. Manalaysay, U. Straumann, and R. Walter, Astron. & Astrophys. **560**, A64 (2013), 1308.6278.
- [55] I. Reiss and U. Keshet, JCAP **2018**, 010 (2018), 1705.05376.
- [56] R. A. Sunyaev and Y. B. Zeldovich, Comments on Astrophysics and Space Physics **4**, 173 (1972).
- [57] M. Birkinshaw, Physics Reports **310**, 97 (1999), astro-ph/9808050.
- [58] J. E. Carlstrom, G. P. Holder, and E. D. Reese, Ann. Rev. Astron. Astrophys. **40**, 643 (2002), astro-ph/0208192.
- [59] J. E. Carlstrom, P. A. R. Ade, K. A. Aird, B. A. Benson, L. E. Bleem, S. Busetto, C. L. Chang, E. Chauvin, H. M. Cho, T. M. Crawford, et al., Pub. Astro. Soc. Pac. **123**, 568 (2011), 0907.4445.
- [60] L. E. Bleem, B. Stalder, T. de Haan, K. A. Aird, S. W. Allen, D. E. Applegate, M. L. N. Ashby, M. Bautz, M. Bayliss, B. A. Benson, et al., Astrophys. J. Suppl. Ser. **216**, 27 (2015), 1409.0850.
- [61] S. Bocquet, J. P. Dietrich, T. Schrabbach, L. E. Bleem, M. Klein, S. W. Allen, D. E. Applegate, M. L. N. Ashby, M. Bautz, M. Bayliss, et al., Astrophys. J. **878**, 55 (2019), 1812.01679.
- [62] J. Song, A. Zenteno, B. Stalder, S. Desai, L. E. Bleem, K. A. Aird, R. Armstrong, M. L. N. Ashby, M. Bayliss, G. Bazin, et al., Astrophys. J. **761**, 22 (2012), 1207.4369.
- [63] J. Ruel, G. Bazin, M. Bayliss, M. Brodwin, R. J. Foley, B. Stalder, K. A. Aird, R. Armstrong, M. L. N. Ashby, M. Bautz, et al., Astrophys. J. **792**, 45 (2014), 1311.4953.
- [64] S. Desai, R. Armstrong, J. J. Mohr, D. R. Semler, J. Liu, E. Bertin, S. S. Allam, W. A. Barkhouse, G. Bazin, E. J. Buckley-Geer, et al., Astrophys. J. **757**, 83 (2012), 1204.1210.
- [65] A. Saro, S. Bocquet, E. Rozo, B. A. Benson, J. Mohr, E. S. Rykoff, M. Soares-Santos, L. Bleem, S. Dodelson, P. Melchior, et al., MNRAS **454**, 2305 (2015), 1506.07814.
- [66] L. E. Bleem, S. Bocquet, B. Stalder, M. D. Gladders, P. A. R. Ade, S. W. Allen, A. J. Anderson, J. Annis, M. L. N. Ashby, J. E. Austermann, et al., Astrophys. J. Suppl. Ser. **247**, 25 (2020), 1910.04121.
- [67] B. A. Benson, P. A. R. Ade, Z. Ahmed, S. W. Allen, K. Arnold, J. E. Austermann, A. N. Bender, L. E. Bleem, J. E. Carlstrom, C. L. Chang, et al., in *Millimeter, Submillimeter, and Far-Infrared Detectors and Instrumentation for Astronomy VII*, edited by W. S. Holland and J. Zmuidzinas (2014), vol. 9153 of *Society of Photo-Optical Instrumentation Engineers (SPIE) Conference Series*, p. 91531P, 1407.2973.
- [68] W. Atwood, A. Albert, L. Baldini, M. Tinivella, J. Bregeon, M. Pesce Rollins, C. Sgrò, P. Bruel, E. Charles, A. Drlica-Wagner, et al. (2013).
- [69] M. Ackermann, M. Ajello, A. Albert, A. Allafort, W. B. Atwood, M. Axelsson, L. Baldini, J. Ballet, G. Barbiellini, D. Bastieri, et al., Astrophys. J. Suppl. Ser. **203**, 4 (2012), 1206.1896.
- [70] M. Wood, R. Caputo, E. Charles, M. Di Mauro, J. Magill, J. S. Perkins, and Fermi-LAT Collaboration, in *35th International Cosmic Ray Conference (ICRC2017)* (2017), vol. 301 of *International Cosmic Ray Conference*, p. 824, 1707.09551.
- [71] J. Ballet, P. Bruel, T. H. Burnett, B. Lott, and The Fermi-LAT collaboration, arXiv e-prints arXiv:2307.12546 (2023), 2307.12546.
- [72] J. R. Mattox, D. L. Bertsch, J. Chiang, B. L. Dingus, S. W. Digel, J. A. Esposito, J. M. Fierro, R. C. Hartman, S. D. Hunter, G. Kanbach, et al., Astrophys. J. **461**, 396 (1996).
- [73] S. S. Wilks, The annals of mathematical statistics **9**, 60 (1938).
- [74] V. Pasumarti and S. Desai, JCAP **2022**, 002 (2022), 2210.12804.
- [75] D. Clowe, M. Bradač, A. H. Gonzalez, M. Markevitch, S. W. Randall, C. Jones, and D. Zaritsky, Astrophys. J. Lett. **648**, L109 (2006), astro-ph/0608407.
- [76] F. Menanteau, J. P. Hughes, C. Sifón, M. Hilton, J. González, L. Infante, L. F. Barrientos, A. J. Baker, J. R. Bond, S. Das, et al., Astrophys. J. **748**, 7 (2012), 1109.0953.
- [77] E. Asencio, I. Banik, and P. Kroupa, Astrophys. J. **954**, 162 (2023), 2308.00744.
- [78] S. Abdollahi, F. Acero, M. Ackermann, M. Ajello, W. B. Atwood, M. Axelsson, L. Baldini, J. Ballet, G. Barbiellini, D. Bastieri, et al., Astrophys. J. Suppl. Ser. **247**, 33 (2020), 1902.10045.
- [79] A. C. Edge, G. C. Stewart, and A. C. Fabian, MNRAS **258**, 177 (1992).

- [80] F. de Gasperin, L. Rudnick, A. Finoguenov, D. Wittor, H. Akamatsu, M. Brüggen, J. O. Chibueze, T. E. Clarke, W. Cotton, V. Cuciti, et al., *Astron. & Astrophys.* **659**, A146 (2022), 2111.06940.
- [81] E. Carretti, S. Brown, L. Staveley-Smith, J. M. Malarecki, G. Bernardi, B. M. Gaensler, M. Havercorn, M. J. Kesteven, and S. Poppi, *MNRAS* **430**, 1414 (2013), 1205.1082.
- [82] C. J. Riseley, A. M. M. Scaife, N. Oozeer, L. Magnus, and M. W. Wise, *MNRAS* **447**, 1895 (2015), 1412.2652.
- [83] H. J. A. Rottgering, M. H. Wieringa, R. W. Hunstead, and R. D. Ekers, *MNRAS* **290**, 577 (1997).
- [84] R. Adam, H. Goksu, A. Leingärtner-Goth, S. Ettori, R. Gnatyk, B. Hnatyk, M. Hütten, J. Pérez-Romero, M. A. Sánchez-Conde, and O. Sergijenko, *Astron. & Astrophys.* **644**, A70 (2020), 2009.05373.
- [85] T. Mauch, T. Murphy, H. J. Buttery, J. Curran, R. W. Hunstead, B. Piestrzynski, J. G. Robertson, and E. M. Sadler, *MNRAS* **342**, 1117 (2003), astro-ph/0303188.
- [86] M. Ajello, R. Angioni, M. Axelsson, J. Ballet, G. Barbiellini, D. Bastieri, J. Becerra Gonzalez, R. Bellazzini, E. Bissaldi, E. D. Bloom, et al., *Astrophys. J.* **892**, 105 (2020), 1905.10771.
- [87] R. Kiuchi, M. Mori, G. V. Bicknell, R. W. Clay, P. G. Edwards, R. Enomoto, S. Gunji, S. Hara, T. Hara, T. Hattori, et al., *Astrophys. J.* **704**, 240 (2009), 0908.3301.
- [88] R. de Menezes, *Astronomy and Computing* **40**, 100609 (2022), 2206.11272.

Cluster Name	RA ($^{\circ}$)	Dec ($^{\circ}$)	M_{500} ($\times 10^{14} M_{\odot}$)/ h)	z	TS Values
SPT-CL J2012-5649	303.11	-56.83	4.85	0.06	37.2
SPT-CL J0431-6126	67.84	-61.44	4.84	0.06	3.0
SPT-CL J2313-4243	348.50	-42.73	4.52	0.06	3.0
SPT-CL J2009-4518	302.45	-45.31	4.20	0.06	2.0
SPT-CL J2201-5956	330.47	-59.94	9.27	0.10	0.6
SPT-CL J0328-5541	52.17	-55.70	5.47	0.08	5.0
SPT-CL J2217-6509	334.49	-65.15	5.34	0.09	2.0
SPT-CL J2249-6426	342.43	-64.43	4.83	0.09	3.0
SPT-CL J0145-5301	26.26	-53.03	5.61	0.11	3.0
SPT-CL J0645-5413	101.37	-54.22	10.05	0.16	1.0
SPT-CL J0500-5116	75.24	-51.27	4.46	0.11	3.0
SPT-CL J2055-5456	313.99	-54.94	5.64	0.14	2.0
SPT-CL J0628-4143	97.20	-41.73	8.46	0.18	3.0
SPT-CL J0404-6510	61.05	-65.18	3.85	0.12	4.0
SPT-CL J0641-5001	100.46	-50.02	3.92	0.12	7.0
SPT-CL J0411-6340	62.86	-63.68	4.85	0.14	3.0
SPT-CL J0145-6033	26.30	-60.56	7.17	0.18	0.5
SPT-CL J2021-5257	305.48	-52.95	4.24	0.14	12.0
SPT-CL J0638-5358	99.70	-53.97	11.29	0.23	2.0
SPT-CL J2012-4130	303.00	-41.50	4.66	0.15	1.5
SPT-CL J0516-6312	79.09	-63.21	4.00	0.14	8.0
SPT-CL J2259-5617	344.00	-56.29	4.71	0.15	3.0
SPT-CL J0027-5015	6.82	-50.25	4.24	0.15	2.5
SPT-CL J0525-4715	81.46	-47.26	7.23	0.19	3.0
SPT-CL J2254-5805	343.59	-58.09	4.47	0.15	3.0
SPT-CL J0537-6504	84.35	-65.07	7.02	0.20	8.5
SPT-CL J0658-5556	104.63	-55.95	15.38	0.30	2.1
SPT-CL J0510-4519	77.58	-45.33	6.94	0.20	3.5
SPT-CL J0637-4829	99.35	-48.49	6.85	0.20	6.3
SPT-CL J2134-4238	323.50	-42.64	6.23	0.19	6.1
SPT-CL J0051-4834	12.79	-48.58	5.69	0.19	2.6
SPT-CL J0317-4849	49.45	-48.83	4.05	0.16	5.1
SPT-CL J2023-5535	305.84	-55.59	7.77	0.23	4.5
SPT-CL J0232-4421	38.07	-44.35	11.29	0.28	6.3
SPT-CL J0216-4816	34.07	-48.28	4.07	0.17	4.7
SPT-CL J2025-5117	306.48	-51.29	6.61	0.22	8.4
SPT-CL J0010-5112	2.74	-51.21	3.91	0.17	2.5
SPT-CL J2254-6314	343.51	-63.25	5.94	0.21	5.8
SPT-CL J2248-4431	342.19	-44.53	15.71	0.35	2.2
SPT-CL J0013-4621	3.47	-46.36	3.91	0.18	5.4
SPT-CL J2020-4646	305.19	-46.77	4.21	0.19	2.0
SPT-CL J0504-4929	76.01	-49.49	4.53	0.20	3.0
SPT-CL J0225-4155	36.48	-41.92	5.20	0.22	2.0
SPT-CL J0458-5741	74.60	-57.70	3.88	0.19	6.3
SPT-CL J2241-4236	340.47	-42.60	4.25	0.20	2.5
SPT-CL J0108-4341	17.13	-43.69	3.83	0.19	3.6
SPT-CL J0124-5937	21.20	-59.63	4.65	0.21	5.0
SPT-CL J0256-4736	44.24	-47.61	5.30	0.23	7.5
SPT-CL J0653-5744	103.33	-57.75	5.71	0.24	3.7
SPT-CL J2211-4833	332.83	-48.56	5.50	0.24	2.5
SPT-CL J0118-5638	19.54	-56.63	4.15	0.21	2.6
SPT-CL J0651-4037	102.82	-40.63	5.15	0.24	5.7
SPT-CL J2121-6335	320.43	-63.58	4.21	0.22	3.2
SPT-CL J0001-6258	0.40	-62.98	3.89	0.21	2.3
SPT-CL J0235-5121	38.95	-51.35	6.56	0.28	1.7
SPT-CL J2005-5635	301.34	-56.59	3.71	0.21	4.7
SPT-CL J2254-4620	343.59	-46.34	5.93	0.27	3.7
SPT-CL J0549-6205	87.33	-62.09	11.65	0.37	3.4
SPT-CL J0516-5430	79.15	-54.51	7.12	0.29	4.6
SPT-CL J2031-4037	307.97	-40.62	9.4	0.34	3.0
SPT-CL J0225-4327	36.30	-43.46	4.25	0.23	3.8
SPT-CL J0040-4407	10.20	-44.13	9.8	0.35	2.2
SPT-CL J0620-4715	95.10	-47.26	4.22	0.23	1.9

TABLE I – continued

SPT-CL J2019-5642	304.77	-56.71	4.05	0.23	5.3
SPT-CL J0249-5658	42.41	-56.98	4.19	0.23	2.1
SPT-CL J0603-4714	90.99	-47.24	5.63	0.27	2.2
SPT-CL J0601-4122	90.50	-41.37	3.92	0.23	4.4
SPT-CL J2138-6008	324.51	-60.13	7.27	0.32	1.0
SPT-CL J2032-5627	308.08	-56.46	5.74	0.28	1.7
SPT-CL J2223-5015	335.81	-50.27	4.06	0.24	2.9
SPT-CL J0412-5106	63.23	-51.11	4.00	0.24	3.9
SPT-CL J2120-4016	320.14	-40.27	4.20	0.25	2.7
SPT-CL J2219-5708	334.96	-57.14	6.30	0.31	4.1
SPT-CL J2300-5331	345.18	-53.52	4.47	0.26	6.0
SPT-CL J2027-4240	306.93	-42.67	3.95	0.25	2.4
SPT-CL J0555-6406	88.87	-64.10	7.64	0.34	6.0
SPT-CL J0311-6354	47.83	-63.91	5.14	0.28	3.1
SPT-CL J0129-6432	22.43	-64.54	6.73	0.32	3.9
SPT-CL J0505-6145	76.40	-61.75	5.15	0.29	8.2
SPT-CL J0133-6434	23.41	-64.57	6.26	0.32	3.4
SPT-CL J2325-4111	351.30	-41.20	7.52	0.36	1.7
SPT-CL J0438-5419	69.57	-54.32	10.28	0.42	4.9
SPT-CL J0405-4916	61.49	-49.27	5.08	0.30	2.1
SPT-CL J2344-4224	356.15	-42.41	3.74	0.26	5.6
SPT-CL J0150-4511	27.65	-45.19	5.28	0.31	1.9
SPT-CL J0041-4428	10.25	-44.48	6.05	0.33	0
SPT-CL J0214-4638	33.70	-46.65	4.90	0.30	5.4
SPT-CL J0143-4452	25.89	-44.87	4.00	0.27	2.9
SPT-CL J0655-5541	103.91	-55.69	4.44	0.29	1.9
SPT-CL J2101-5542	315.31	-55.70	3.82	0.27	3.0
SPT-CL J0440-4657	70.23	-46.97	5.05	0.31	2.0
SPT-CL J0106-5943	16.62	-59.72	6.40	0.35	4.3
SPT-CL J2130-6458	322.73	-64.98	5.23	0.32	4.2
SPT-CL J0439-4600	69.81	-46.01	5.58	0.33	4.4
SPT-CL J2011-5725	302.85	-57.42	3.99	0.28	5.6
SPT-CL J0348-4515	57.07	-45.25	6.33	0.36	3.2
SPT-CL J0304-4921	46.06	-49.36	7.53	0.39	5.2
SPT-CL J0455-4159	73.99	-41.99	4.01	0.29	6.1
SPT-CL J2223-5227	335.87	-52.47	4.00	0.29	1.3
SPT-CL J2115-4659	318.80	-46.99	4.25	0.30	4.2
SPT-CL J2016-4954	304.01	-49.91	3.91	0.29	2.6
SPT-CL J0522-4818	80.57	-48.30	4.08	0.30	6.3
SPT-CL J0151-5654	27.79	-56.91	3.86	0.29	3.1
SPT-CL J0234-5831	38.68	-58.52	7.93	0.41	4.5
SPT-CL J0114-4123	18.68	-41.39	7.03	0.39	4.3
SPT-CL J0022-4144	5.55	-41.74	4.05	0.30	3.2
SPT-CL J0411-4819	62.82	-48.32	8.04	0.42	3.0
SPT-CL J0551-4339	87.88	-43.66	4.82	0.33	3.7
SPT-CL J2355-5055	358.95	-50.93	4.49	0.32	3.9
SPT-CL J0509-6118	77.47	-61.31	6.65	0.39	4.9
SPT-CL J0636-4942	99.17	-49.70	5.40	0.35	7.5
SPT-CL J0110-4445	17.59	-44.76	5.57	0.36	3.0
SPT-CL J0013-4906	3.33	-49.12	7.12	0.41	3.9
SPT-CL J0001-4842	0.28	-48.71	4.48	0.33	3.7
SPT-CL J0217-5245	34.30	-52.76	4.82	0.34	11.9
SPT-CL J0254-5857	43.57	-58.95	7.72	0.44	3.1
SPT-CL J2330-4502	352.57	-45.03	4.06	0.32	4.1
SPT-CL J0304-4401	46.07	-44.03	8.37	0.46	2.8
SPT-CL J0236-4938	39.25	-49.64	4.42	0.33	2.1
SPT-CL J0600-4353	90.06	-43.88	5.08	0.36	3.8
SPT-CL J0052-5657	13.16	-56.96	3.92	0.32	2.5
SPT-CL J0650-4503	102.68	-45.06	6.22	0.40	6.6
SPT-CL J2059-5018	314.93	-50.30	4.05	0.33	4.8
SPT-CL J2131-4019	322.77	-40.32	7.49	0.45	2.8
SPT-CL J0416-6359	64.16	-63.99	4.47	0.35	4.7
SPT-CL J0424-4406	66.00	-44.11	4.73	0.36	4.6
SPT-CL J0240-5946	40.16	-59.77	5.79	0.40	8.4
SPT-CL J0144-4807	26.18	-48.12	3.84	0.33	2.7
SPT-CL J0405-4648	61.29	-46.81	4.70	0.36	3.7

TABLE I – continued

SPT-CL J2358-6129	359.71	-61.49	4.45	0.36	4.4
SPT-CL J2135-5726	323.92	-57.44	6.31	0.43	7.6
SPT-CL J0330-5228	52.73	-52.47	6.75	0.44	3.6
SPT-CL J0412-5743	63.02	-57.72	3.98	0.34	4.3
SPT-CL J2332-5358	353.11	-53.97	5.55	0.40	2.3
SPT-CL J0012-5352	3.06	-53.87	3.91	0.34	4.3
SPT-CL J2205-5927	331.27	-59.46	4.35	0.37	2.8
SPT-CL J2344-4243	356.18	-42.72	11.38	0.60	5.8
SPT-CL J0402-4611	60.58	-46.19	4.07	0.36	3.5
SPT-CL J0052-4551	13.19	-45.86	4.06	0.36	3.5
SPT-CL J0243-4833	40.91	-48.56	7.74	0.50	2.2
SPT-CL J2022-6323	305.53	-63.40	4.56	0.38	4.7
SPT-CL J2327-5137	351.78	-51.62	3.55	0.34	3.7
SPT-CL J2316-5453	349.21	-54.90	4.24	0.37	5.1
SPT-CL J0344-5518	56.21	-55.30	3.89	0.36	2.6
SPT-CL J2145-5644	326.47	-56.75	6.97	0.48	5.2
SPT-CL J2233-5339	338.33	-53.65	5.82	0.44	2.8
SPT-CL J2159-6244	329.99	-62.74	4.54	0.39	3.6
SPT-CL J0445-4230	71.28	-42.51	5.05	0.41	3.5
SPT-CL J0551-5709	87.90	-57.16	5.28	0.42	1.2
SPT-CL J2124-6124	321.15	-61.41	5.47	0.43	4.8
SPT-CL J2351-5452	357.90	-54.88	4.25	0.38	1.9
SPT-CL J2206-4057	331.62	-40.95	3.70	0.36	5.4
SPT-CL J0252-4824	43.19	-48.41	5.04	0.42	7.6
SPT-CL J0429-4355	67.31	-43.93	3.83	0.37	5.3
SPT-CL J2259-5431	344.98	-54.53	4.23	0.39	3.9
SPT-CL J0025-5034	6.37	-50.57	3.85	0.37	8.3
SPT-CL J0447-5055	71.84	-50.92	4.29	0.40	2.8
SPT-CL J0019-4051	4.76	-40.86	6.18	0.48	3.2
SPT-CL J2136-4704	324.12	-47.08	4.78	0.43	1.7
SPT-CL J0354-5904	58.56	-59.07	4.57	0.42	3.8
SPT-CL J0333-5842	53.32	-58.70	3.59	0.37	1.8
SPT-CL J0244-4857	41.03	-48.96	4.41	0.41	2.4
SPT-CL J0342-4028	55.56	-40.48	4.92	0.44	5.3
SPT-CL J2030-5638	307.70	-56.64	3.97	0.39	2.9
SPT-CL J0509-5342	77.34	-53.71	5.35	0.46	8.5
SPT-CL J2319-4716	349.98	-47.28	4.54	0.43	2.9
SPT-CL J0611-5938	92.81	-59.64	3.77	0.39	6.3
SPT-CL J0054-4046	13.59	-40.78	4.11	0.40	5.7
SPT-CL J0505-4204	76.37	-42.08	3.89	0.40	5.6
SPT-CL J0655-5234	103.96	-52.57	5.42	0.47	2.8
SPT-CL J0334-4659	53.55	-46.99	5.76	0.49	3.3
SPT-CL J2016-4517	304.00	-45.30	3.86	0.40	5.0
SPT-CL J2342-4714	355.75	-47.24	3.81	0.40	5.8
SPT-CL J0047-4506	11.82	-45.11	5.24	0.47	4.2
SPT-CL J0439-5330	69.93	-53.50	4.06	0.41	6.5
SPT-CL J0647-5828	101.98	-58.48	4.64	0.44	6.1
SPT-CL J0341-5027	55.28	-50.46	3.59	0.39	2.2
SPT-CL J0254-6051	43.60	-60.86	4.60	0.44	5.7
SPT-CL J2140-5727	325.14	-57.46	3.87	0.40	9.0
SPT-CL J0452-4806	73.00	-48.11	3.47	0.38	3.1
SPT-CL J0259-4556	44.90	-45.94	4.28	0.43	4.6
SPT-CL J0626-4446	96.74	-44.77	4.50	0.44	3.9
SPT-CL J0237-4151	39.42	-41.86	3.78	0.41	2.2
SPT-CL J2035-5251	308.80	-52.85	6.38	0.53	4.6
SPT-CL J0014-4036	3.74	-40.60	6.14	0.52	3.0
SPT-CL J0257-5842	44.39	-58.71	3.91	0.42	2.3
SPT-CL J0638-4243	99.57	-42.72	3.71	0.41	6.9
SPT-CL J0417-4748	64.35	-47.81	7.41	0.58	5.0
SPT-CL J0655-4429	103.76	-44.48	3.72	0.41	6.1
SPT-CL J0543-6219	85.76	-62.32	5.53	0.51	4.3
SPT-CL J2335-4544	353.79	-45.74	6.38	0.55	5.3
SPT-CL J2306-6505	346.73	-65.09	5.96	0.53	6.6
SPT-CL J0611-4724	92.92	-47.41	4.23	0.45	3.9
SPT-CL J2112-4434	318.21	-44.58	5.86	0.53	6.6
SPT-CL J0038-5244	9.72	-52.74	3.83	0.43	7.9

TABLE I – continued

SPT-CL J2111-5339	317.92	-53.65	4.20	0.44	3.2
SPT-CL J0351-5636	57.93	-56.61	3.48	0.41	3.2
SPT-CL J0546-4752	86.55	-47.88	3.94	0.43	4.7
SPT-CL J2050-4213	312.57	-42.22	5.14	0.50	5.2
SPT-CL J0200-4852	30.14	-48.88	5.11	0.50	2.6
SPT-CL J0216-4830	34.07	-48.51	4.52	0.47	5.5
SPT-CL J0346-5439	56.72	-54.65	5.72	0.53	3.2
SPT-CL J2259-3952	344.81	-39.87	5.84	0.54	2.9
SPT-CL J0257-4817	44.45	-48.30	3.89	0.44	7.4
SPT-CL J0451-4952	72.97	-49.88	3.63	0.42	3.6
SPT-CL J0532-5450	83.03	-54.84	3.72	0.43	4.5
SPT-CL J0317-5935	49.32	-59.59	4.41	0.47	1.9
SPT-CL J0257-5732	44.35	-57.54	3.73	0.43	2.1
SPT-CL J2235-4416	338.86	-44.27	4.03	0.45	4.5
SPT-CL J0517-6311	79.41	-63.20	3.90	0.45	6.7
SPT-CL J0403-5719	60.97	-57.32	4.18	0.47	4.3
SPT-CL J0456-6141	74.15	-61.68	3.60	0.44	4.2
SPT-CL J0314-6130	48.61	-61.51	3.51	0.43	1.7
SPT-CL J0508-6149	77.16	-61.82	3.73	0.45	7.2
SPT-CL J0641-5950	100.38	-59.85	5.01	0.52	6.8
SPT-CL J0417-4427	64.41	-44.46	5.81	0.56	5.8
SPT-CL J0307-5042	46.95	-50.70	5.55	0.55	3.9
SPT-CL J0232-5257	38.19	-52.96	5.63	0.56	11.5
SPT-CL J0124-4301	21.15	-43.02	3.92	0.47	9.0
SPT-CL J2132-4349	323.17	-43.83	4.82	0.52	6.8
SPT-CL J2131-5003	322.97	-50.06	3.81	0.46	3.9
SPT-CL J0102-4915	15.73	-49.26	13.52	0.87	4.7
SPT-CL J0113-6105	18.40	-61.09	3.63	0.45	3.0
SPT-CL J0304-4748	46.15	-47.81	4.56	0.51	4.0
SPT-CL J2331-5051	352.96	-50.86	5.81	0.58	3.5
SPT-CL J0544-3950	86.25	-39.84	4.78	0.52	3.2
SPT-CL J0048-4548	12.25	-45.80	3.79	0.47	3.8
SPT-CL J0007-4706	1.75	-47.11	3.64	0.46	6.4
SPT-CL J0306-4749	46.75	-47.82	3.64	0.46	4.2
SPT-CL J0337-6300	54.47	-63.01	3.76	0.46	2.0
SPT-CL J0111-5424	17.77	-54.41	4.06	0.48	3.7
SPT-CL J0456-5116	74.17	-51.28	5.39	0.56	2.7
SPT-CL J0257-6050	44.34	-60.85	3.54	0.46	3.9
SPT-CL J0659-5300	104.77	-53.01	3.89	0.48	0
SPT-CL J2145-4348	326.36	-43.80	4.03	0.49	0
SPT-CL J0253-6046	43.46	-60.77	3.64	0.46	0
SPT-CL J2302-4435	345.58	-44.58	3.61	0.47	0
SPT-CL J2245-6206	341.26	-62.11	5.67	0.59	0
SPT-CL J0337-4928	54.45	-49.47	3.94	0.49	0
SPT-CL J2232-5959	338.15	-59.99	5.81	0.60	5.3
SPT-CL J2040-5342	310.22	-53.71	4.44	0.52	4.3
SPT-CL J0559-5249	89.92	-52.83	5.97	0.61	4.1
SPT-CL J0307-6225	46.83	-62.43	5.36	0.58	3.8
SPT-CL J0025-4133	6.49	-41.55	4.64	0.54	3.3
SPT-CL J0109-4045	17.47	-40.76	3.61	0.48	2.5
SPT-CL J0238-4904	39.70	-49.07	4.18	0.52	1.9
SPT-CL J0221-4446	35.42	-44.78	3.85	0.50	5.7
SPT-CL J2051-6256	312.80	-62.93	3.61	0.48	3.8
SPT-CL J0218-4315	34.58	-43.26	6.00	0.63	3.8
SPT-CL J0106-5355	16.57	-53.92	3.78	0.50	1.8
SPT-CL J0219-4934	34.81	-49.58	4.52	0.55	3.5
SPT-CL J0111-5518	17.84	-55.31	3.54	0.49	3.2
SPT-CL J0351-4109	57.75	-41.16	5.69	0.61	4.6
SPT-CL J2017-6258	304.48	-62.98	4.27	0.54	5.1
SPT-CL J2148-6116	327.18	-61.28	4.82	0.57	2.5
SPT-CL J0619-5802	94.92	-58.04	4.51	0.55	10.3
SPT-CL J0135-5902	23.79	-59.04	3.79	0.51	6.1
SPT-CL J0041-5107	10.29	-51.13	3.62	0.50	4.0
SPT-CL J0342-5354	55.52	-53.91	3.90	0.51	3.8
SPT-CL J0135-5904	23.97	-59.08	3.52	0.49	5.2
SPT-CL J0343-5518	55.76	-55.30	4.19	0.54	3.2

TABLE I – continued

SPT-CL J0033-6326	8.48	-63.44	5.08	0.60	4.8
SPT-CL J0212-4657	33.10	-46.95	6.06	0.65	5.5
SPT-CL J0410-6343	62.52	-63.73	3.95	0.53	3.8
SPT-CL J0336-4005	54.16	-40.10	3.76	0.52	5.6
SPT-CL J0217-4310	34.41	-43.18	4.55	0.57	4.0
SPT-CL J2218-4519	334.75	-45.32	5.60	0.64	4.8
SPT-CL J0429-5233	67.43	-52.56	3.39	0.50	3.1
SPT-CL J2337-5942	354.35	-59.70	8.29	0.77	5.2
SPT-CL J2155-6048	328.98	-60.81	3.95	0.54	3.0
SPT-CL J2350-5301	357.73	-53.02	3.95	0.54	2.6
SPT-CL J0542-4100	85.72	-41.00	5.48	0.64	3.4
SPT-CL J2222-4834	335.71	-48.57	5.69	0.65	3.6
SPT-CL J0522-5026	80.52	-50.44	3.60	0.52	5.5
SPT-CL J0309-4958	47.26	-49.97	4.07	0.55	0
SPT-CL J0202-5401	30.58	-54.02	4.07	0.55	0
SPT-CL J0426-5455	66.52	-54.92	5.43	0.64	3.6
SPT-CL J0142-5032	25.55	-50.54	6.05	0.68	5.3
SPT-CL J0402-6130	60.71	-61.50	3.51	0.52	2.9
SPT-CL J0011-4614	2.98	-46.24	3.88	0.54	6.2
SPT-CL J2155-5224	328.89	-52.41	3.95	0.55	5.9
SPT-CL J0444-4352	71.17	-43.87	3.69	0.53	5.0
SPT-CL J2020-6314	305.03	-63.24	3.74	0.54	5.2
SPT-CL J0030-5213	7.53	-52.22	3.62	0.53	5.5
SPT-CL J0512-5139	78.16	-51.66	4.11	0.57	6.6
SPT-CL J0152-5303	28.23	-53.05	4.70	0.61	2.0
SPT-CL J2206-5807	331.66	-58.13	4.51	0.60	3.6
SPT-CL J0157-4007	29.45	-40.13	4.12	0.57	5.4
SPT-CL J0649-4510	102.45	-45.17	3.85	0.55	6.0
SPT-CL J0543-4250	85.94	-42.84	4.85	0.62	2.0
SPT-CL J2110-5244	317.55	-52.75	4.56	0.61	1.7
SPT-CL J0243-5930	40.86	-59.51	4.92	0.64	3.0
SPT-CL J0217-5014	34.27	-50.24	3.52	0.54	3.0
SPT-CL J0256-5617	44.10	-56.30	4.83	0.63	2.5
SPT-CL J2312-4621	348.06	-46.35	4.68	0.63	1.3
SPT-CL J2354-5633	358.71	-56.55	3.73	0.56	1.8
SPT-CL J2220-4534	335.08	-45.58	4.77	0.64	4.1
SPT-CL J0519-4248	79.85	-42.81	3.71	0.57	2.2
SPT-CL J0422-5140	65.59	-51.68	4.01	0.59	4.3
SPT-CL J2140-5331	325.03	-53.52	3.66	0.57	3.5

TABLE I: The TS values for SPT-SZ Galaxy Clusters along with their masses and redshifts. The clusters are arranged in the decreasing order of their M_{500}/z^2 values. The clusters with $TS > 9$ corresponding to at least 3σ significance are shown in bold text.